nature communications

Article

https://doi.org/10.1038/s41467-025-67334-y

Field-effect passivation for minimized voltage loss in highly efficient antimony selenosulfide solar cells

Received: 8 August 2025

Accepted: 27 November 2025

Published online: 06 January 2026

Check for updates

Anwen Gong[1], Cong Liu[1] ✉, Jiexi Yang[1], Binghuan Li[1], Shilin Yang[1], Rongshan Yang[1], Yousheng Wang[2], Kai Shen[2], Qifan Xue[3], Zhiqiang Li[4], Jing Wang[5] ✉, Bingsuo Zou[1] ✉ & Yaohua Mai[2] ✉

The inferior heterojunction quality and misaligned energy levels at the buffer/absorber interface cause severe interface recombination and large open-circuit voltage (V_{OC}) loss, limiting the power conversion efficiency (PCE) of antimony selenosulfide ($Sb_2(S,Se)_3$) solar cells. Here, we develop a field-effect passivation strategy by introducing a low-work-function Ta_2O_5 dielectric layer between the CdS and $Sb_2(S,Se)_3$ layers. This Ta_2O_5 layer serves as an optimal substrate for growing highly crystalline $Sb_2(S,Se)_3$ films while also enhancing interfacial charge transport. The positive fixed charges in Ta_2O_5 strengthen the built-in electric field and promotes electrons extraction while suppressing holes accumulation at the interface, thereby substantially suppressing non-radiative recombination probabilities. Implementing this passivation strategy yields a record PCE of 10.95% (10.65% certified) an V_{OC} of 695 mV, corresponding to a remarkably low voltage deficit. This work establishes a universal physical passivation paradigm for interface quality optimization and V_{OC} loss mitigation in high-performance $Sb_2(S,Se)_3$ photovoltaics.

In response to the depletion of traditional energy sources, there has been a growing demand for clean and renewable energy, driving the development of new thin-film solar cells. Antimony selenosulfide ($Sb_2(S,Se)_3$) has recently demonstrated significant potential in emerging thin-film photovoltaics due to its high stability, low toxicity, tunable band gap and excellent optoelectronic properties[1–4]. Based on these advantages, $Sb_2(S,Se)_3$ solar cells have undergone a rapid development, achieving a reported power conversion efficiency (PCE) of 10.92%[5]. However, the current efficiency of these thin-film solar cells is limited by significant open-circuit voltage (V_{OC}) losses caused by severe non-radiative recombination at the absorber layer and interfaces[6,7]. Currently, high-efficiency $Sb_2(S, Se)_3$ solar cells are often fabricated through direct deposition on cadmium sulfide (CdS) substrates. An unfavorable energy level arrangement at the $CdS/Sb_2(S,Se)_3$ interface, such as a cliff-like band structure, can cause severe carrier recombination at the interface. Therefore, developing an efficient passivation strategy to improve the quality of the $CdS/Sb_2(S,Se)_3$ heterojunction and mitigate the V_{OC} losses of devices is crucial.

Researchers have conducted extensive studies on interface engineering to improve the quality of heterojunctions and suppress interface carrier recombination. To transform the band structure at the $CdS/Sb_2(S,Se)_3$ interface from a cliff-like to spike-like structure, Liu et al. employed a heterojunction lithiation strategy and achieved a high PCE of 10.76% for the $Sb_2(S,Se)_3$ solar cells[8]. As for optimizing the CdS

[1]Guangxi Key Laboratory of Processing for Non-ferrous Metals and Featured Materials, School of Resources, Environment and Materials, Guangxi University, Nanning, China. [2]Institute of New Energy Technology, College of Physics & Optoelectronic Engineering, Jinan University, Guangzhou, China. [3]State Key Laboratory of Luminescent Materials and Devices, South China University of Technology, Guangzhou, China. [4]National-Local Joint Engineering Laboratory of New Energy Photoelectric Devices, College of Physics Science and Technology, Hebei University, Baoding, China. [5]School of Materials and Energy, Guangdong University of Technology, Guangzhou, China. ✉e-mail: congliu@gxu.edu.cn; jingwang777@gdut.edu.cn; zoubs@gxu.edu.cn; yaohuamai@jnu.edu.cn

buffer layer, a hydrazine hydrate solution was used to remove surface oxides and improve the surface morphology of CdS films, resulting in a PCE of 10.30%[9]. Besides, Chen group investigated the effects of potassium chloride (KCl) and ethylenediamine (EDA) post-treatments on CdS films, which yielded PCEs of 9.98% and 10.10%, respectively[10,11]. They found that KCl treatment effectively reduced the surface roughness of CdS films and improved their conductivity, while EDA treatment promoted the grain growth and crystallinity of CdS films and suppressed the formation of interface defects. Although these passivation approaches reduced the V_{OC} losses of the device to some extent, such chemically-based passivation methods suffer from byproduct residues, poor long-term stability and potentially harmful chemical reactions at interfaces. This hinders the reproducibility of device performance and large-scale applications[12].

In addition to chemical passivation technology, a physical passivation strategy, such as field-effect passivation by introducing a dielectric layer, is a promising approach. In crystalline silicon (Si) solar cells, the zinc oxide (ZnO), titanium oxide (TiO_2), strontium oxide (SrO_x) thin films have been deposited on the Si substrate to provide moderate surface passivation and form the additional interfacial fields, which facilitate the charge-selective transport and reduce the probability of interface recombination[13–15]. In perovskite solar cells, a molybdenum oxide (MoO_x) thin film with a high work function is inserted between the perovskite and hole transport layer. This field-effect passivation of MoO_x effectively enhances the built-in field and improves interface charge transport thanks to the formation of interfacial polarization[16]. Furthermore, fixed charge passivation is used to modify carrier concentration distribution near the heterojunctions and selectively extract charge carriers[17,18]. Despite these advantages, the application of the physical passivation strategy to inorganic thin-film solar cells remains underexplored, and the impact of field-effect passivation on the charge transport and recombination dynamics in $Sb_2(S,Se)_3$ solar cells has rarely been reported.

Herein, we fabricated an ultrathin, transparent Ta_2O_5 dielectric layer between CdS and $Sb_2(S,Se)_3$ layers to investigate the effect of field-effect passivation on the V_{OC} loss in the device. Ta_2O_5 is a wide-bandgap transition metal oxide that exhibits exceptional optical transparency and chemical stability[19,20]. Its material properties remain unaffected during subsequent high-temperature hydrothermal and annealing processes. There are positive fixed charges generated in Ta_2O_5 films, which can attract electrons while concurrently repelling holes away from the interface[21]. Thanks to the reduced V_{OC} losses resulting from this field-effect passivation, the champion device achieves a certified PCE of 10.65% with V_{OC} of 692 mV, corresponding to 54.96% of the theoretical limit ($V_{OC}/V_{OC,SQ}$), which is comparable to the highest reported value (55.14%) for $Sb_2(S,Se)_3$ solar cells[5]. This type of inorganic thin-film solar cells also exhibits good operational stability.

Results and discussion

Characterization of CdS/Ta_2O_5 buffer layers

In this study, a highly transparent and ultrathin Ta_2O_5 dielectric layer was fabricated via the sol-gel spin-coating technique. Fig. 1a depicts the specific reaction pathway and conditions for Ta_2O_5:Ta^{5+} ions in the solution form ethanol-tantalum complexes preferentially, followed by the generation of the desired Ta_2O_5 precipitate under the influence of high temperature and hydroxyl groups. The inset shows the transparent, homogeneous Ta_2O_5 precursor solution. To demonstrate the formation of Ta_2O_5, X-ray diffraction (XRD) was conducted on the thin-film samples to determine their composition and crystal structure. As shown in the XRD pattern, all diffraction peaks of the sample closely match the orthorhombic phase of Ta_2O_5 (JCPDS #25-0922), with a pronounced (001) grain orientation. The Ta_2O_5 dielectric layer has a high dielectric constant of ~28[22], a wide band gap of 4.25 eV (Supplementary Fig. 1), and an ultralow electrical conductivity of ~ 2.11×10^{-5} S/cm based on Hall effect measurements. Scanning electron microscopy (SEM) analysis of CdS films without and with Ta_2O_5 modification revealed distinct morphological characteristics. As shown in Fig. 1b, e, the pure CdS films exhibited a rougher surface morphology with numerous pinholes. Such low-quality seed layers can degrade the quality of subsequent $Sb_2(S,Se)_3$ films and the resultant device performance. Remarkably, the deposition of Ta_2O_5 effectively filled surface pinholes and cracks in the CdS films, resulting in a smoother and more uniform surface topography. To verify the uniformity of the ultrathin Ta_2O_5 layer, we performed EDS mapping analysis on the CdS/Ta_2O_5 substrate. As shown in Supplementary Fig. 2, the Ta signal (representing Ta_2O_5) exhibits a continuous and homogeneous distribution on the surface of CdS films, with no observable island-like aggregation or large-scale uncovered areas. This indicates a uniform and complete coverage of the CdS film by the deposited Ta_2O_5 layer. Simultaneously, the signals of Cd and S also display a homogeneous distribution, further confirming that the Ta_2O_5 layer is sufficiently ultra-thin, thereby allowing the underlying CdS signals to remain clearly detectable. The CdS and CdS/Ta_2O_5 films exhibited similar transmittance across the entire visible spectrum (Supplementary Fig. 3). We also used atomic force microscopy (AFM) to analyse the surface morphology of CdS films (Fig. 1c, f). Following the deposition of Ta_2O_5, the roughness (R_q) of the CdS films was decreased from 27.8 nm to 23.1 nm, consistent with the SEM results. We also conducted the contact angle tests on CdS films (Fig. 1d). The contact angle was reduced from 61.9° to 44.0° after the Ta_2O_5 layer was introduced, positively impacting the heterogeneous nucleation and grain growth of the $Sb_2(S,Se)_3$ films. To confirm that the Ta_2O_5 layer facilitates carrier transport, we measured the conductivity of CdS films, and the results are shown in Fig. 1g (the inset shows the structure of device). After depositing the Ta_2O_5 dielectric layer, the conductivity of the CdS films was increased from 3.74×10^{-5} S/cm to 6.22×10^{-5} S/cm.

Morphological analysis of $Sb_2(S,Se)_3$ layer

According to previous studies, the polarity of CdS surfaces has a significant influence on the growth orientation of the absorber layer[1]. As shown in Supplementary Fig. 4, the $Sb_2(S,Se)_3$ films tend to form a favorable (hk1) grain orientation on the non-polar (100) plane of CdS films. In contrast, exposure of the polar (101) and (10$\bar{1}$) planes leads to complex anisotropy in the grain orientation of $Sb_2(S,Se)_3$, negatively affecting the carrier transport. To demonstrate that the Ta_2O_5 layer reduces the exposure of polar planes in CdS, we performed XRD measurements on CdS films. As shown in the Supplementary Fig. 5, compared to the pure CdS film, the CdS/Ta_2O_5 sample exhibits significantly reduced peak intensities of polar planes, such as (101), and enhanced peak intensities of nonpolar planes, such as (100)[23]. To investigate the effect of Ta_2O_5 dielectric layer on the quality of $Sb_2(S,Se)_3$ films, we implemented XRD and SEM measurements. The diffraction patterns of $Sb_2(S,Se)_3$ films matched well with the orthorhombic Sb_2S_3 (JCPDS#42-1393) and Sb_2Se_3 (JCPDS#15-0861) phases (Supplementary Fig. 6a). We calculated the texture coefficients (TC) of the crystal planes for $Sb_2(S,Se)_3$ films deposited on CdS and CdS/Ta_2O_5 substrates based on the XRD data, with detailed results presented in Supplementary Fig. 6b[24]. The $Sb_2(S,Se)_3$ films deposited on the CdS/Ta_2O_5 substrate exhibit significantly higher TC values for (*hk*1) planes, such as (211), (221), (301) and (421) compared to those of the control $Sb_2(S,Se)_3$ films. This provides evidence for the optimized grain orientation of $Sb_2(S,Se)_3$ films induced by the Ta_2O_5 layer. As shown in Supplementary Fig. 7, the local XRD analysis revealed that $Sb_2(S,Se)_3$ films deposited on Ta_2O_5 substrates exhibited stronger (hk1) diffraction peaks and narrower full width at half maximum than the control $Sb_2(S,Se)_3$ films. Regarding the slight shift in diffraction peaks, we attribute it to the changes in the chemical composition of the absorber layer (Supplementary Fig. 8 and Supplementary Table 1).

https://doi.org/10.1038/s41467-025-67334-y

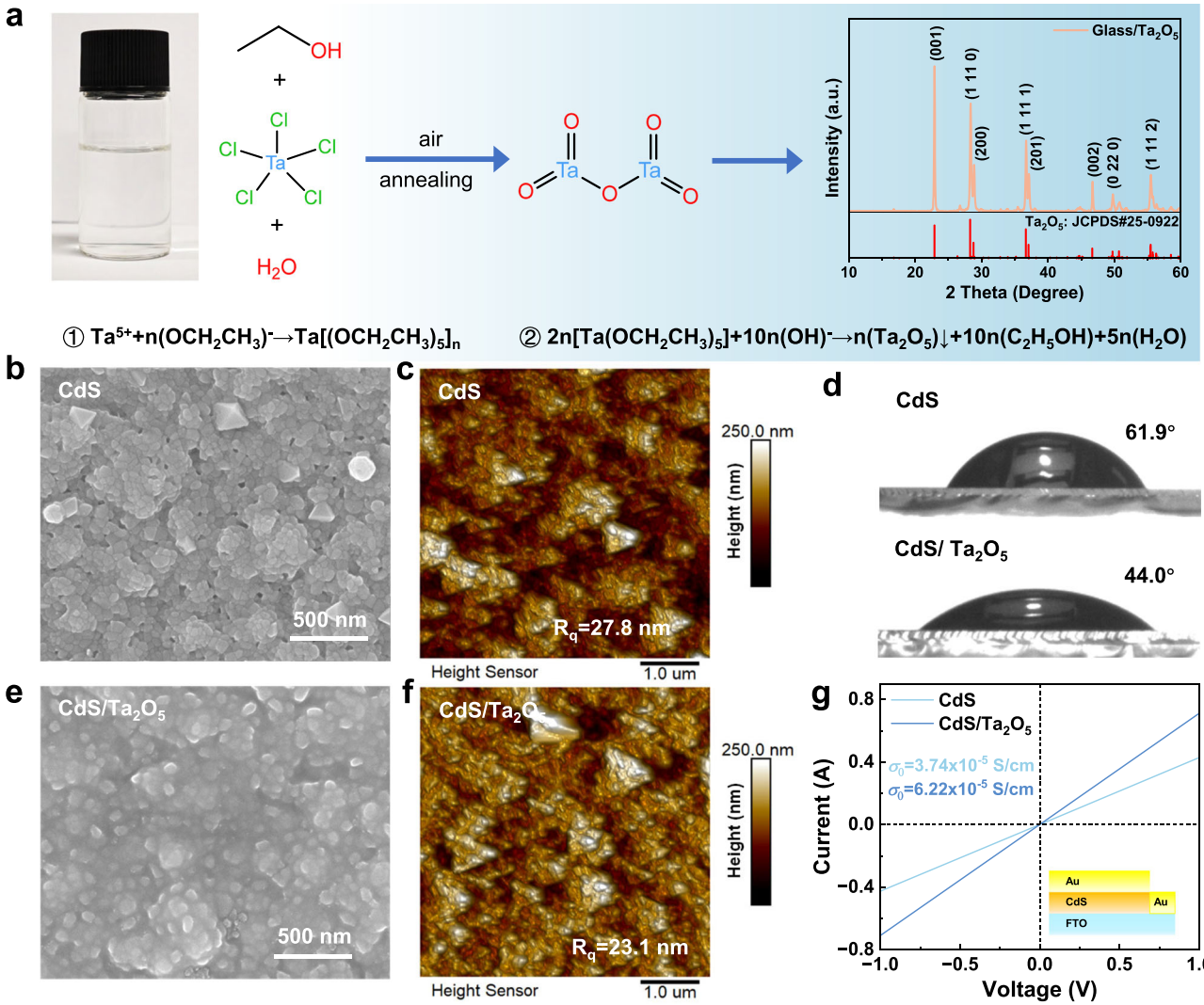

Fig. 1 | Characterization of CdS/Ta_2O_5 buffer layers. a Reaction schematic and XRD pattern of Ta_2O_5 (The inset shows the precursor solution of Ta_2O_5). **b**, **e** Scanning electron microscopy (SEM) images, **c**, **f** atomic force microscopy (AFM) mappings, and **d** hydrophilicity measurements of CdS and CdS/Ta_2O_5 films. **g** *I*–*V* characteristics of FTO/CdS/Au and FTO/CdS/Ta_2O_5/Au devices for conductivity evaluation.

The introduction of Ta_2O_5 substrate modifies the crystallization kinetics, leading to an altered S/Se ratio in $Sb_2(S,Se)_3$[25]. SEM images reflected that both the control and Ta_2O_5-modified $Sb_2(S,Se)_3$ films had a compact morphology. However, the control films displayed a higher density of large granular precipitates, and the phenomenon was effectively mitigated in the Ta_2O_5-modified $Sb_2(S,Se)_3$ films. Supplementary Fig. 9 showcased the AFM images of the $Sb_2(S,Se)_3$ films, indicating that the R_q was reduced for films deposited on Ta_2O_5 substrate (39.6 nm) compared to that of the control films (50.3 nm). We attributed this to the suppression of large granular precipitates in the absorber layer. The reduced surface roughness facilitates uniform interfacial contact and minimizes localized recombination, which is critical for enhancing charge transport and device performance. These results suggest that the insertion of Ta_2O_5 layer improves the crystallinity, grain orientation and morphology of $Sb_2(S,Se)_3$ films. Therefore, the $Sb_2(S,Se)_3$ films deposited on Ta_2O_5 substrate exhibit an enhanced light absorption due to the improved film quality (Supplementary Fig. 10). Since interfacial stability is fundamental to device reproducibility and long-term reliability, we performed HAADF-STEM imaging and corresponding EDS mapping analysis for a cross-sectional sample with structure of FTO/CdS/Ta_2O_5/$Sb_2(S,Se)_3$. As shown in Supplementary Fig. 11, the HAADF-STEM image reveals sharp and distinct interfaces between all functional layers. Notably, a continuous thin layer with a thickness of ~3 nm, corresponding to Ta_2O_5, is clearly observed between the CdS and $Sb_2(S,Se)_3$ layers. EDS mapping further demonstrates a sharp and confined Ta signal precisely at the CdS/$Sb_2(S,Se)_3$ interface, while other elements such as Cd, S, Sb, and Se exhibit negligible interdiffusion. These results confirm that the Ta_2O_5 dielectric layer maintains robust chemical and structural stability during high-temperature hydrothermal and annealing processes, forming well-defined heterointerfaces with adjacent layers.

Fixed charge passivation

In crystalline silicon solar cells, Ta_2O_5 has been widely recognized as an efficient passivation layer, which is capable of introducing fixed charges at the silicon surface. Theoretically, when Ta_2O_5 contacts with $Sb_2(S,Se)_3$ layer, it may exhibit a similar fixed charge effect. To validate our analyses, we measured the fixed charges by preparing the metal oxide semiconductor (MOS) structured devices for *C*–*V* measurements (Fig. 2a). By differentiating the *C*–*V* data, the voltage corresponding to the extreme value represents the flat-band voltage. As shown in Fig. 2b, the flat-band voltages of the CdS and CdS/Ta_2O_5 samples are −0.35 V and −0.50 V, respectively. We therefore confirm that the Ta_2O_5 enables

https://doi.org/10.1038/s41467-025-67334-y

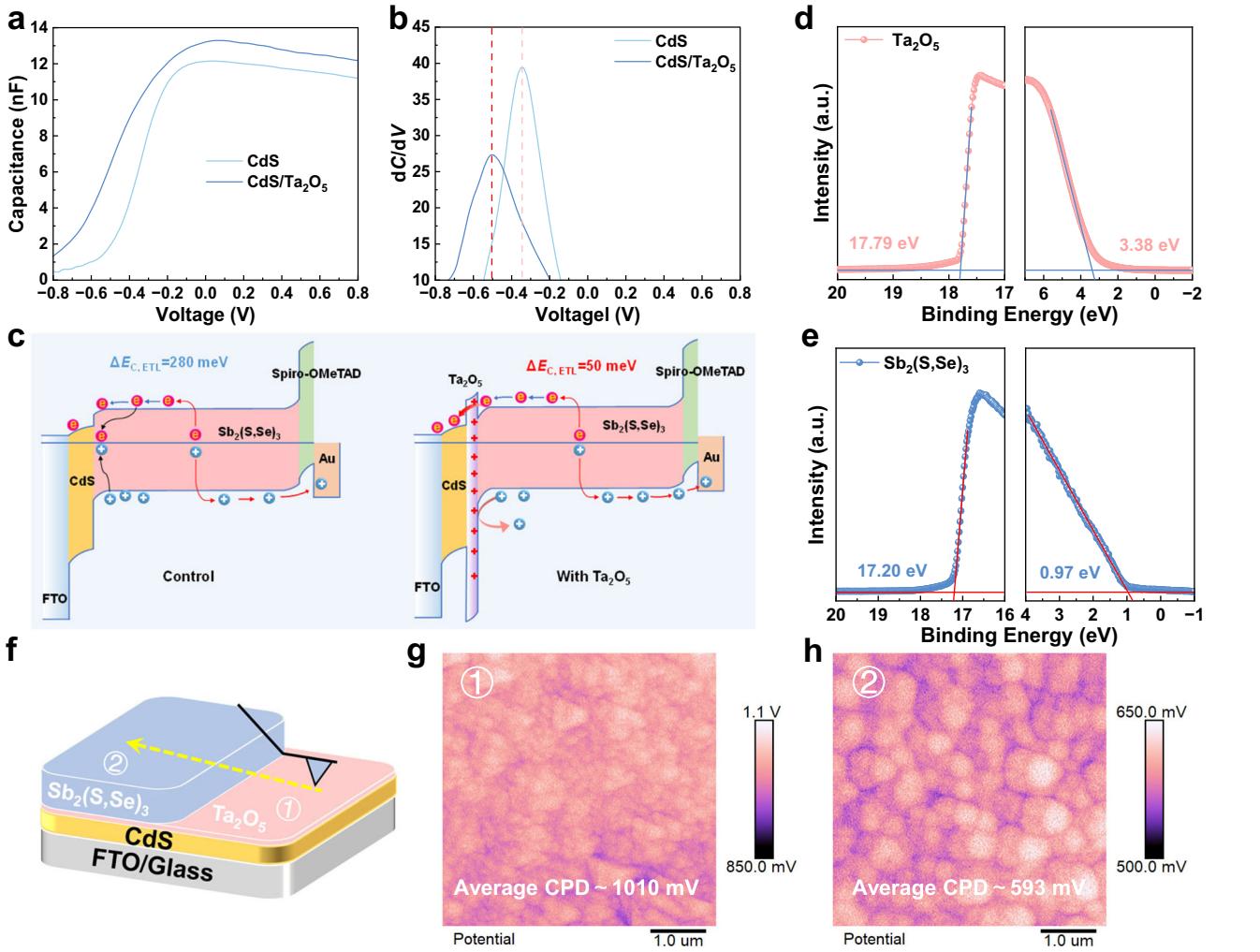

Fig. 2 | Fixed charge passivation. a *C–V* curves and **b** flat band voltage of CdS and CdS/Ta_2O_5 devices. The *C–V* measurements were performed on devices with the structures FTO/CdS/$Sb_2(S,Se)_3$/Au and FTO/CdS/Ta_2O_5/$Sb_2(S,Se)_3$/Au. **c** Schematic band diagrams of the control and Ta_2O_5 incorporated devices. UPS spectra of secondary electron cutoff and valence band of (**d**) Ta_2O_5 and **e** $Sb_2(S,Se)_3$ films. **f** Schematic diagram of the KPFM measurements. **g**, **h** The corresponding KPFM images of regions 1 and 2.

positive fixed charges at the interface, consistent with reported literatures[26,27]. The fixed charge (Q_f) density was calculated using the following formula[28]:

$$Q_f = \frac{C_{in}(V_{MS} - V_{fb})}{A \times q} \quad (1)$$

Here, C_{in} denotes the intrinsic capacitance of the MOS structure, V_{MS} represents the metal-semiconductor potential difference determined by the work function difference between FTO (4.8 eV) and $Sb_2(S,Se)_3$, V_{fb} is the flat-band voltage, A is the electrode area, and q is the elementary charge. The calculated fixed charge density Q_f of the Ta_2O_5 layer is $+2.24 \times 10^{11}\,cm^{-2}$ (Supplementary Table 2). When positive fixed charges of Ta_2O_5 appear at the interface, more electrons of $Sb_2(S,Se)_3$ gather therein, resulting in a downward band bending of $Sb_2(S,Se)_3$ (Fig. 2c). These positive fixed charges enable field-effect passivation at the Ta_2O_5/$Sb_2(S,Se)_3$ interface, facilitating efficient electron extraction and suppressing hole accumulation[17,18]. To theoretically verify the field-effect passivation mechanism of the Ta_2O_5 layer, we performed the device simulations by using the SCAPS-1D software[29,30]. A device model is established that accurately corresponds to the actual structure of solar cells. All the essential materials parameters are shown in Supplementary Table 3. The simulation results (Supplementary Fig. 12) demonstrate that the insertion of the Ta_2O_5 layer significantly reduces the conduction band offset ($\Delta E_{C,ETL}$) between CdS and $Sb_2(S,Se)_3$ from 280 to 50 meV. The Ta_2O_5 layer provides a more favorable path for efficient transport of photogenerated electrons from the absorber layer to the electron transport layer.

In addition to the fixed positive charges, Fermi level alignment between Ta_2O_5/$Sb_2(S,Se)_3$ also results in band bending with the same trend. We performed the ultraviolet photoelectron spectroscopy (UPS) for the Ta_2O_5 and $Sb_2(S,Se)_3$ films, respectively. Fig. 2d, e present that the secondary electron cut-off edges are 17.79 and 17.20 eV, and the distances between Fermi energy level and valence band maximum are 3.38 and 0.97 eV for the Ta_2O_5 and $Sb_2(S,Se)_3$, respectively. The corresponding work functions are 3.43 eV and 4.02 eV, similar to the values reported in the literature[11,18]. As shown in Fig. 2c, the band bending of $Sb_2(S,Se)_3$ is downward while the band bending of Ta_2O_5 is upward when the Fermi-level alignment is achieved between Ta_2O_5/$Sb_2(S,Se)_3$. Kelvin probe force microscopy (KPFM) was conducted to probe the contact potential difference (CPD) across the Ta_2O_5/$Sb_2(S,Se)_3$ heterojunction (Fig. 2f). A significant reduction in CPD was observed as the probe traversed from the Ta_2O_5 region to the $Sb_2(S,Se)_3$ region (Fig. 2g, h). The Ta_2O_5 region exhibited an average

https://doi.org/10.1038/s41467-025-67334-y

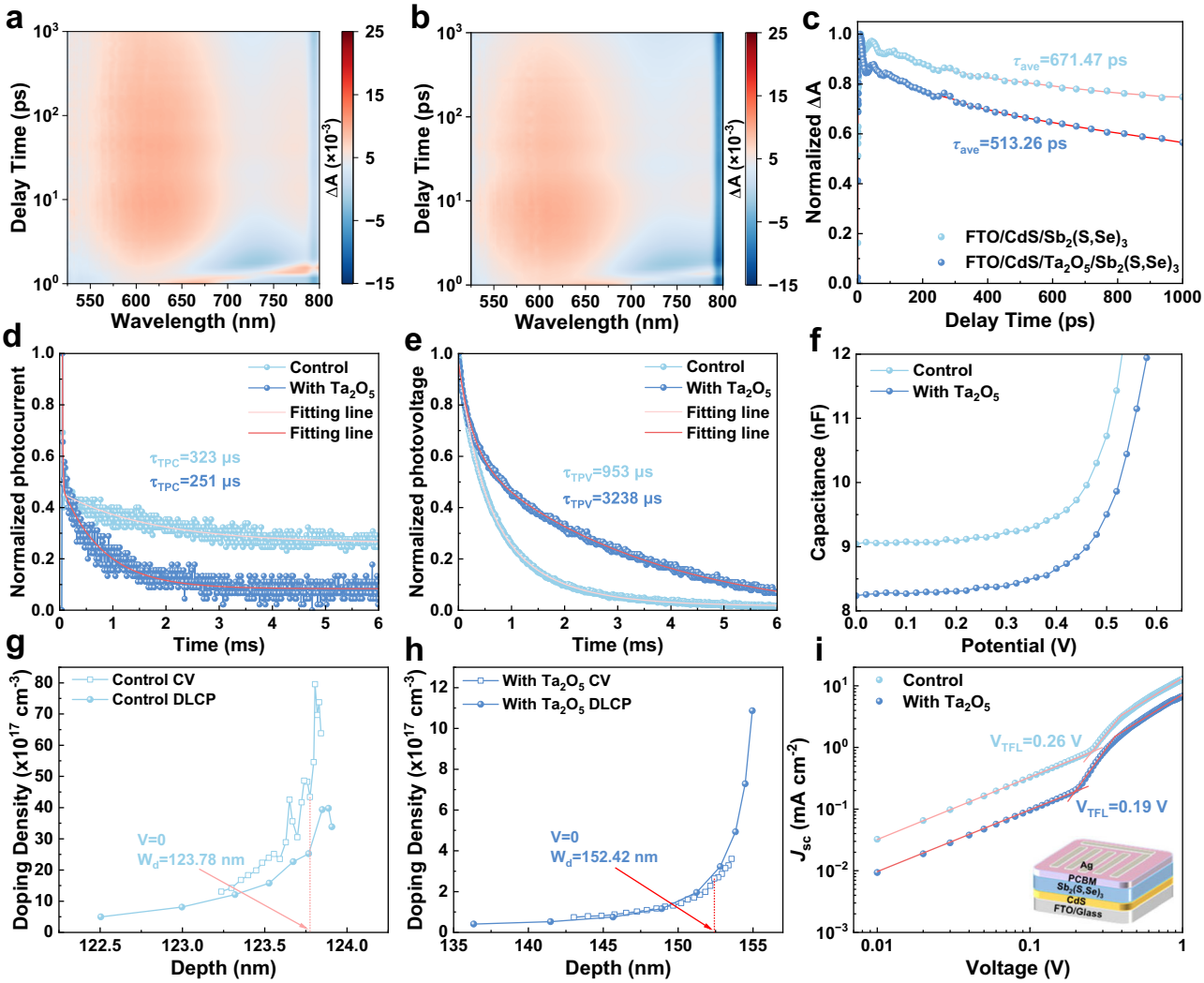

Fig. 3 | Carrier dynamics and interfacial defect analysis. Two-dimensional pseudo-color images of TAS spectra of the (**a**) FTO/CdS/$Sb_2(S,Se)_3$ and **b** FTO/CdS/Ta_2O_5/$Sb_2(S,Se)_3$ samples. **c** Transient decay kinetics of the $Sb_2(S,Se)_3$ films deposited on CdS and CdS/Ta_2O_5 substrate. **d**, **e** Transient photovoltage/photocurrent (TPV/TPC) curves, **f** capacitance–voltage (*C–V*) curves, **g**, **h** *C–V* and *DLCP* profiles, and **i** space charge limiting current (SCLC) curves for the control and Ta_2O_5 incorporated devices.

CPD of approximately 1010 mV, while the $Sb_2(S,Se)_3$ region exhibited a decreased CPD of approximately 593 mV. This difference in CPD is consistent with the UPS analysis. With the insertion of Ta_2O_5 layer, the presence of fixed positive charges and the significant work function difference induce more pronounced downward band bending of $Sb_2(S,Se)_3$.

Carrier dynamics and interfacial defect study

To further verify that the Ta_2O_5 dielectric layer facilitated carrier transport, we used transient absorption spectroscopy (TAS) to analyze the carrier transport dynamics. Fig. 3a, b showcased the two-dimensional pseudo-color maps of the TAS spectra for $Sb_2(S,Se)_3$ films. Broad photo-induced absorption (PIA, $\Delta A > 0$) in the range of 525–700 nm appeared in both samples due to the formation of $S^{\bullet-}$ radical and the trapping of holes within $Sb_2(S,Se)_3$ films[31,32]. Compared to the control samples, the $Sb_2(S,Se)_3$ films deposited on Ta_2O_5 dielectric layer exhibited lower PIA signals. Supplementary Fig. 13 displayed the time-resolved absorption spectra at different times, in which the Ta_2O_5 incorporated $Sb_2(S,Se)_3$ films showed a weaker peak intensity than the control films at the same delay time. In general, the TAS intensity reflects the number of carriers in the conduction and valence bands of the absorber, so the decreased intensity can be attributed to the effective charge transport via the Ta_2O_5 dielectric layer[33]. Fig. 3c showed the decay kinetics of the photobleaching peak intensity at 622 nm for the samples, and the carrier decay lifetimes were obtained by fitting the double-exponential equations in Supplementary Note 1. The corresponding results were listed in Supplementary Table 4. The average carrier decay lifetimes of the $Sb_2(S,Se)_3$ films on the Ta_2O_5 layer are much lower than those of the control films, suggesting that Ta_2O_5 layer enables the fast electron extraction and transportation to cathode. To explore the carrier recombination behavior, we performed the transient photovoltage/photocurrent (TPV/TPC) measurements on the devices without and with Ta_2O_5 dielectric layers. As shown in Fig. 3d and Supplementary Table 5, the TPC results indicated a reduced photocurrent decay lifetime of 252 μs in the Ta_2O_5 incorporated devices compared to that of the control devices (328 μs), consistent with the analysis of TAS measurements. Fig. 3e presented the TPV decay curves of the devices, in which the Ta_2O_5 incorporated devices exhibited a longer carrier recombination lifetime of 3238 μs than that of the control devices (953 μs) (Supplementary Table 5). We attributed this to the suppressive carrier recombination rate by the field-effect passivation of Ta_2O_5. Additionally, the capacitance-voltage (*C-V*) measurements showed a decreased capacitance in the Ta_2O_5 incorporated devices (Fig. 3f). This suggests

https://doi.org/10.1038/s41467-025-67334-y

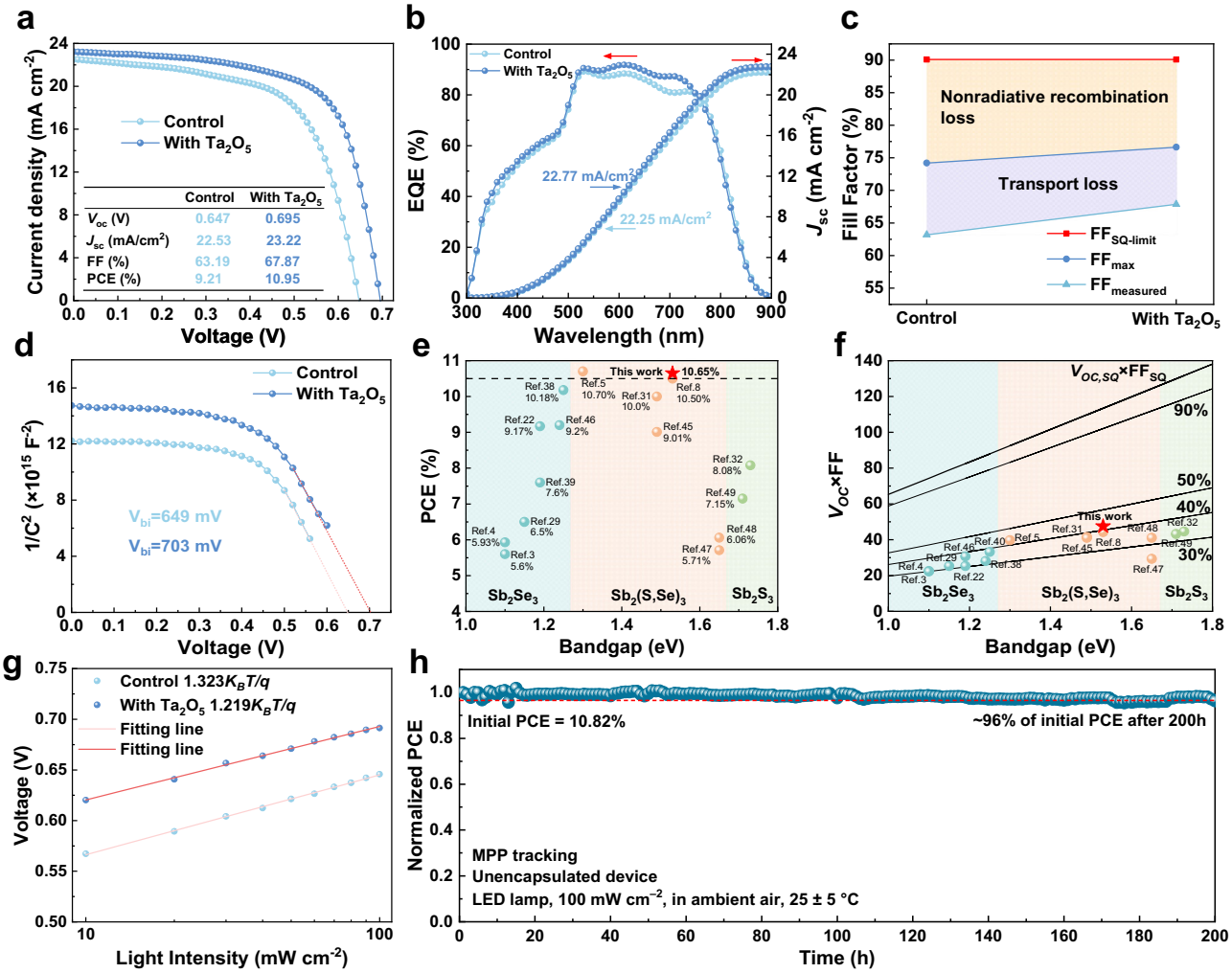

Fig. 4 | Device performance and characterization. a *J*–*V* curves and **b** EQE spectra of the control and champion devices. **c** Fill factor (FF) loss analysis for control, and Ta_2O_5 incorporated devices. **d** Capacitance-voltage (*C*–*V*) curves for control and Ta_2O_5 incorporated devices. **e** Certified efficiencies for Sb-based chalcogenide solar cells. The dashed line indicates the benchmark PCE of 10.5%. **f** Certified V_{OC} × FF versus absorber bandgap for Sb-based chalcogenide solar cells from published literature. Solid lines denote Shockley-Queisser limits ($V_{OC,SQ}$ × FF_{SQ}) at different percentiles for corresponding band gaps. **g** Light-intensity-dependent V_{OC} for control and Ta_2O_5 incorporated devices. **h** Maximum power point (MPP) tracking of the unencapsulated device with the Ta_2O_5 dielectric layer under ambient conditions.

that the Ta_2O_5 dielectric layer can effectively suppress the aggregation of carriers at the CdS/$Sb_2(S,Se)_3$ interface and reduce the probability of carrier recombination[34], which is in agreement with the results of the TPV measurements.

We performed *C*–*V* and DLCP measurements on the devices without and with Ta_2O_5 layer to explore the interface defects in the CdS/$Sb_2(S,Se)_3$ heterojunction. The defect density from *C*–*V* measurements (N_{CV}) includes the free carriers, bulk defects, and interfacial defects, and the defect density from DLCP measurements (N_{DLCP}) contains the free carriers and bulk defects[4,35]. Therefore, the interfacial defects can be determined by the difference between the N_{CV} and N_{DLCP}. The defect densities of the devices were calculated according to the equation in Supplementary Note 2, and the corresponding results were shown in Supplementary Table 6. Compared to the control devices, the Ta_2O_5 incorporated devices exhibited a lower interfacial defect density and a wider depletion region (Fig. 3g, h). This was due to the introduction of Ta_2O_5 improved the morphology and hydrophilicity of CdS films, providing a favorable substrate for the deposition of high-quality $Sb_2(S,Se)_3$ films. The defect density and electron mobility are further investigated by the *J*–*V* curves according to the space-charge limited current model. Figure 3i displayed the dark *J*–*V* curves of the electron-only devices without and with Ta_2O_5, and the defect densities were calculated according to the formulas in Supplementary Note 3. The insertion of Ta_2O_5 reduced the electron defect densities of the devices from 6.91×10^{15} to 5.05×10^{15} cm^{-3}. Moreover, the Ta_2O_5 incorporated devices exhibit a higher electron mobility compared to that of control devices (Supplementary Fig. 14), demonstrating that the Ta_2O_5 dielectric layer effectively enhances electron extraction and collection. We conclude that the Ta_2O_5 dielectric layer not only improves the charge transport dynamics at the interface but also achieves a high-quality CdS/$Sb_2(S,Se)_3$ heterojunction with fewer interface defects.

Device performance and characterization

Encouraged by the field-effect passivation of Ta_2O_5, we fabricated the solar cells with the device structure of FTO/CdS/Ta_2O_5/$Sb_2(S,Se)_3$/Spiro-OMeTAD/Au. The influence of Ta_2O_5 layers with different thickness on device performance was analyzed, and the corresponding current density-voltage (*J*–*V*) curves and device parameters were shown in Supplementary Fig. 15 and Supplementary Table 7. As expected, the introduction of Ta_2O_5 dielectric layers with varying thickness significantly improved photovoltaic performance. Fig. 4a showcased the *J*–*V* curves of the control and champion Ta_2O_5

Table 1 | Summary of the certified photovoltaic parameters of the $Sb_2(S,Se)_3$ solar cells

Ref.	E_g (eV)	V_{OC} (V)	FF (%)	PCE (%)	$V_{OC}/V_{OC,\ SQ}$ (%)	V_{OC}×FF (%)
Nat. Photon. (2015)[3]	1.1	0.4	55.7	5.6	46.61	22.28
Nat. Energy (2017)[4]	1.1	0.391	57.8	5.93	45.56	22.6
Nat. Energy (2025)[5]	1.3	0.576	68.96	10.7	55.14	39.72
Energy Environ. Sci. (2024)[8]	1.53	0.672	65.9	10.5	53.38	44.28
Angew. Chem. Int. Ed. (2025)[24]	1.19	0.47	65.36	9.17	49.89	30.72
ACS Energy Lett. (2017)[29]	1.15	0.427	59.3	6.5	47.19	25.32
Nat. Energy (2020)[31]	1.49	0.655	63.5	10	53.61	41.59
Adv. Energy Mater. (2025)[32]	1.73	0.692	64.45	8.08	47.88	44.6
Energy Environ. Sci. (2024)[38]	1.25	0.477	69.63	10.18	47.8	33.21
Nat. Commun. (2018)[39]	1.19	0.42	60.4	7.6	44.58	25.37
Chem. Eng. J. (2022)[45]	1.49	0.61	67.3	9.01	49.93	41.05
Nat. Commun. (2019)[46]	1.24	0.4	70.3	9.2	40.46	28.12
Sol. RRL (2017)[47]	1.65	0.56	52.4	5.71	40.85	29.34
Adv. Electron. Mater. (2019)[48]	1.65	0.744	55.19	6.06	54.27	41.06
Adv. Energy Mater. (2022)[49]	1.71	0.703	61.46	7.15	49.27	43.21
This work	**1.53**	**0.692**	**68.70**	**10.65**	**54.96**	**47.54**

incorporated devices measured under AM 1.5 G illumination (100 mW cm^{-2}). The control devices achieved a PCE of 9.21% with a V_{OC} of 0.647 V, a short circuit current density (J_{SC}) of 22.53 mA cm^{-2} and a fill factor (FF) of 63.19%. Specifically, the devices with optimal thickness of Ta_2O_5 reached a PCE of 10.95% with a V_{OC} of 0.695 V, a J_{SC} of 23.22 mA cm^{-2} and a FF of 67.87%, which is the highest efficiency for the Sb-based thin-film solar cells so far. Besides, the *J*–*V* curves simulated by SCAPS-1D show significant improvements in V_{OC} and FF (Supplementary Fig. 16 and Supplementary Table 8), which are fully consistent with our experimental results. Moreover, the Ta_2O_5 incorporated devices exhibited a good reproducibility (Supplementary Fig. 17). Fig. 4b showed the external quantum efficiency (EQE) of the control and Ta_2O_5 incorporated devices, and the integrated current densities are in good agreement with J_{SC} obtained from the *J*–*V* curves. The response in the spectral range of 330–500 nm is enhanced due to the optimization of the CdS buffer layer and the heterojunction interface, while the response in the spectral range of 500–750 nm is increased because of the improved quality of $Sb_2(S,Se)_3$ absorber layer[36]. We further calculated the Urbach energy of the devices based on the EQE spectra. As shown in Supplementary Fig. 18, the Ta_2O_5 incorporated devices displayed a reduced Urbach energy of 28.43 meV compared to 31.47 meV for the control devices. The lower Urbach energy indicates that the $Sb_2(S,Se)_3$ films deposited on Ta_2O_5 layers have a higher crystallinity and less bulk defects[37,38].

To investigate the impact of the Ta_2O_5 dielectric layer on the FF of devices, we decomposed the FF losses into non-radiative recombination losses and transport losses through Supplementary Note 4 (Fig. 4c and Supplementary Table 9). The theoretical maximum fill factor (FF_{max}) values for the control and Ta_2O_5 incorporated devices were 74.2% and 76.64%, respectively. Introducing the Ta_2O_5 dielectric layer reduced FF losses caused by non-radiative recombination from 19.90% to 13.16%. The optical band gaps calculated from EQE measurements show no variation between the control and Ta_2O_5 incorporated devices (Supplementary Fig. 19). This indicates that the improvement of V_{OC} is due to the field-effect passivation of Ta_2O_5 and the increased built-in electric field of devices. As shown in the capacitance–voltage (C^{-2}–V) curves, the extracted built-in voltage (V_{bi}) of the control devices is 649 mV, which is increased to 703 mV for the Ta_2O_5 incorporated devices (Fig. 4d). Furthermore, the optimized devices were submitted to an authoritative, independent laboratory (South China National Center of Metrology) for performance certification (certification report provided in Supplementary Fig. 20). Consequently, the Ta_2O_5 incorporated devices demonstrated a certified PCE of 10.65% (10.57%) with a V_{OC} of 0.692 (0.691) V, a FF of 68.70% (68.17%) and a J_{SC} of 22.42 (22.45) mA cm^{-2} measured in reverse (forward) scan. It is worth noting that the certified PCE of 10.65% is second only to the certified record efficiency of 10.70% (Fig. 4e and Table 1). As shown in Fig. 4f (calculation method detailed in Supplementary Note 5), we calculated the product of $V_{OC,SQ} \times FF_{SQ}$ according to the Shockley-Queisser limit values across different band gaps, and compared the $V_{OC} \times FF$ values of the reported certified devices. The product of $V_{OC} \times FF$ in this work reached 47.54%, which was the highest value among all the reported certified devices (Table 1). Concurrently, the $V_{OC}/V_{OC,SQ}$ ratio of the certified device attained 54.96%, indicating a substantially reduced V_{OC} deficit ($V_{OC,\ def}$) (Supplementary Fig. 21 and Table 1). These results fully demonstrated the effectiveness of the field-effect passivation strategy in enhancing device performance.

To further demonstrate that carrier recombination was suppressed, we implemented the dark *J*–*V* characterization, light-intensity-dependent *J*–*V* measurements, and electrical impedance spectroscopy (EIS) under both dark and different light intensity conditions. It can be seen in Supplementary Fig. 22a that the reverse leakage currents were significantly reduced upon the incorporation of Ta_2O_5 layer. By processing and fitting the dark *J*–*V* curves based on the equations in Supplementary Note 6, we can obtain relevant device parameters, including shunt conductance (G), series resistance (R_S), diode ideality factor (A) and reverse saturation current density (J_0). As shown in Supplementary Fig. 22b-d, the Ta_2O_5 incorporated devices exhibit a G value of 0.0005 mS cm^{-2}, an R_S of 2.55 Ω cm^2, a diode ideality factor of 1.78 and a J_0 of 6.28×10^{-6} mA cm^{-2}. All these parameters show improvement over those of the control device, which had a G value of 0.006 mS cm^{-2}, an R_S of 6.43 Ω cm^2, a diode ideality factor of 1.92 and a J_0 of 2.48×10^{-5} mA cm^{-2}. We then measured the V_{OC} versus light-intensity curves that followed the relationship of $V_{OC}/n(k_BT/q)$ ln (I), where the k_B, T, and q represent Boltzmann's constant, the temperature in Kelvin, and the elementary charge, respectively. In the case of ideal trap-free recombination, the slope of the curves corresponds to k_BT/q. Any deviation of the measured slope from k_BT/q indicates the extent of trap-assisted recombination under open-circuit conditions[39]. As shown in Fig. 4g, the Ta_2O_5 incorporated devices exhibit a lower slope of 1.219 k_BT/q than that of the control devices (1.323 k_BT/q), indicating that the Ta_2O_5 layer suppresses trap-assisted recombination at the $CdS/Sb_2(S,Se)_3$ interfaces through the effective field-effect passivation. Furthermore, the light-intensity dependence of J_{SC} (Supplementary Fig. 23) also demonstrates that the introduction of the Ta_2O_5 dielectric layer effectively suppresses carrier recombination in the

devices. We performed EIS on the devices without and with Ta_2O_5 dielectric layer under dark conditions (Supplementary Fig. 24). The starting point in the high-frequency region represents the series resistance R_S, and the semicircle arc in the low-frequency region denotes the recombination resistance R_{rec}. The extracted R_S of solar cells decreased from 19.79 to 3.35 Ω and the R_{rec} increased from 1358.85 to 4676.42 Ω with the introduction of Ta_2O_5 dielectric layer. To investigate the interfacial charge transfer properties of the devices, we performed EIS measurements under different light intensities. As shown in Supplementary Fig. 25a, b, all the Nyquist plots exhibit a single semicircular arc, indicating that the interfacial process is dominated by a single time constant[40]. The equivalent circuit model was used to fit the impedance data (Supplementary Fig. 25c), where R_S represents the series resistance, R_{ct} corresponds to the charge transfer resistance, and the constant phase element denotes the geometric capacitive behavior of the device[41]. The R_{ct} value of both devices decreases linearly with the increasing light intensity (Supplementary Fig. 25d), which can be attributed to that the increased photogenerated carrier concentration effectively reduces the energy barrier of charge transfer. Notably, the R_{ct} values of the Ta_2O_5 incorporated device were significantly lower than those of the control device under different light intensities. This demonstrates that the fixed charges in the Ta_2O_5 dielectric layer effectively reduce the charge transfer barrier through the field-effect passivation effect, thereby promoting efficient extraction and transport of charge carriers[42–44]. Clearly, the Ta_2O_5 incorporated devices exhibit enhanced electrical properties and suppressed carrier recombination in comparison to the control devices, accounting for the improvement of V_{OC} and FF[45]. Finally, we performed the stability measurement of an unencapsulated target device that maintained ~96% of its initial PCE after continuous tracking at maximum power point for 200 h, demonstrating good operational stability (Fig. 4h).

Discussion

In summary, we have demonstrated a physical passivation strategy by introducing a low work function Ta_2O_5 dielectric layer between the CdS and $Sb_2(S,Se)_3$ layers, to promote charge transfer and suppress carrier recombination at interfaces. The introduction of Ta_2O_5 not only realizes a twofold optimization of the CdS buffer layer and the $Sb_2(S,Se)_3$ absorber layer, but also yields a field-effect passivation at the CdS/$Sb_2(S,Se)_3$ heterojunction. This strategy improves the built-in potential of the devices and provides additional driving force for extracting electron-carrier to the cathode and mitigating hole–carrier accumulation at the interface, which effectively reduces the non-radiative recombination losses and the V_{OC} deficit. By this strategy, the optimized $Sb_2(S,Se)_3$ solar cell achieved a PCE of 10.95% with a high V_{OC} of 695 mV and a FF of 67.87%, which also reached a certified efficiency of 10.65% with a V_{OC} of 692 mV and a FF of 68.70%. This study reveals that field-effect passivation induced by fixed charges effectively improves carrier transport dynamics and heterojunction quality, which can be extended to other electronic devices.

Methods

Materials

All chemicals in this work were used as received without further purification unless otherwise specified. Cadmium nitrate tetrahydrate ($Cd(NO_3)_2{\cdot}4H_2O$, AR), ammonium hydroxide (NH_4OH, 25–28%), thiourea (CH_4N_2S, GR), Cadmium chloride hemipentahydrate ($CdCl_2{\cdot}2.5H_2O$, AR), antimony potassium tartrate ($C_4H_4KO_7Sb{\cdot}0.5H_2O$, CP), and sodium thiosulfate pentahydrate ($Na_2S_2O_3{\cdot}5H_2O$, AR) were purchased from Sinopharm Chemical Reagent Co., Ltd. Tantalum(V) chloride ($TaCl_5$, 99.99%) was obtained from Macklin. Selenourea (CH_4N_2Se, 98%) and acetonitrile (C_2H_3N, 99.8%) were sourced from Sigma-Aldrich Trading Co., Ltd. Lithium bis(trifluoromethanesulfonyl) imide (Li-TFSI, 99%) and Spiro-OMeTAD (99.9%) were procured from Yolight Solar Technology Co., Ltd. 4-tert-Butylpyridine (tBP, 96%) and ethanol (C_2H_6O, 99.8%) were acquired from Aladdin Biochemical Technology Co., Ltd.

Devices fabrications

Fabrication of Ta_2O_5 dielectric layer: The fabrication process initiated by dissolving 10 mg tantalum chloride ($TaCl_5$) in 1.8 mL ethanol with 30 min ultrasonication. Subsequently, 1.12 mL ethanol and 0.08 mL ultrapure water were added to the solution, followed by another 30 min ultrasonication. The homogenized mixture was filtered through a 200 nm membrane filter to remove large aggregates, after which 1 mL ethanol was introduced and magnetically stirred for 1 h to obtain the Ta_2O_5 precursor solution. This precursor (50 µL) was then spin-coated onto CdS substrates at varying spin speeds (4000–6000 rpm) and thermally annealed at 400–600 °C for 5 min under ambient air conditions, ultimately yielding densely compacted Ta_2O_5 films. The thicknesses of the Ta_2O_5 films prepared by different spin speeds were determined by spectroscopic ellipsometry to be 1 ± 0.5, 3 ± 0.5 and 5 ± 0.5 nm, respectively.

Fabrication of $Sb_2(S,Se)_3$ solar cells: The cleaned FTO substrates were first treated with UV-ozone for 20 min, followed by CdS film deposition via chemical bath deposition at 66 °C for 16.5 min. The CdS precursor solution was prepared by thoroughly mixing 20 mL cadmium nitrate tetrahydrate ($Cd(NO_3)_2{\cdot}4H_2O$), 26 mL ammonium hydroxide (NH_4OH, 25–28%), 14 mL thiourea (CH_4N_2S), and 140 mL ultrapure water. A cadmium chloride methanol solution (20 mg/mL) was then spin-coated onto the CdS film at 3000 rpm for 30 s and annealed in air at 400 °C for 10 min to complete the CdS buffer layer. Subsequently, Ta_2O_5 dielectric layers with varying thicknesses were fabricated on the CdS surface. For the deposition of $Sb_2(S,Se)_3$ absorber layer, antimony potassium tartrate ($C_4H_4KO_7Sb{\cdot}0.5H_2O$), sodium thiosulfate pentahydrate ($Na_2S_2O_3{\cdot}5H_2O$), and selenourea (CH_4N_2Se) served as Sb, S, and Se sources. Specifically, 0.260 g antimony potassium tartrate was dissolved in 39 mL ultrapure water, followed by sequential addition of 0.774 g sodium thiosulfate and 19.2 mg selenourea to form the precursor solution. The solution was transferred into a Teflon-lined autoclave containing FTO/CdS or FTO/CdS/Ta_2O_5 substrates and hydrothermally deposited at 135 °C for 2 h. Post annealing was conducted at 400 °C for 10 min under a nitrogen atmosphere to enhance the crystallinity of $Sb_2(S,Se)_3$. Spiro-OMeTAD hole transport layers were fabricated by thoroughly mixing 36.6 mg Spiro-OMeTAD, 29 µL 4-tert-butylpyridine (tBP), 9.5 µL lithium bis(-trifluoromethanesulfonyl)imide (Li-TFSI, 520 mg/mL in acetonitrile), and 1 mL chlorobenzene, followed by spin-coating at 2000 rpm for 30 s under ambient conditions and subsequent annealing at 100 °C for 10 min. Device fabrication was finalized through thermal evaporation of an approximately 80 nm Au back electrode.

Characterization

Scanning electron microscopy (SEM, TESCAN MIRA LMS) was used to analyze the surface morphology of the CdS and $Sb_2(S,Se)_3$ films. The surface roughness and CPD were measured using a Bruker Multimode 8 equipped with an AFM and a KPFM. The absorption and transmission spectra were measured by a spectrophotometer (UV-2600i). The crystal structure of the $Sb_2(S,Se)_3$ films was measured by an X-ray diffractometer (XRD, Bruker D8 Discover) with a radiation source of Cu kα. The energy level structures of Ta_2O_5 and $Sb_2(S,Se)_3$ films were measured by UV photoelectron spectroscopy (UPS, Thermo Fisher Scientific ESCALAB Xi) at −5 V bias. Core energy level variations of different elements in Ta_2O_5 and $Sb_2(S,Se)_3$ films were analyzed using an X-ray photoelectron spectrometer (XPS, Thermo Scientific Nexsa). Femtosecond TAS of $Sb_2(S,Se)_3$ films was tested using a pumped probe system (Helios, Ultrafast System LLC). TPC, TPV, EIS, and C^{-2}-V curves were measured using a Zahner electrochemical workstation. C–V and DLCP measurements were conducted

using a Keithley 4200 semiconductor characterization system on device structures of Glass/FTO/CdS/without or with Ta_2O_5/$Sb_2(S,Se)_3$/Spiro-OMeTAD/Au. The *C–V* measurements were performed in the dark at room temperature with an alternating current (AC) amplitude of 30 mV, a frequency of 100 kHz and a direct current (DC) bias voltage range of 1 to 0.3 V. DLCP measurements were performed with an AC amplitude range of 15 to 140 mV and a DC bias voltage range of −0.2 to 0.2 V. The *J–V* curves of the devices were measured by combining a standard xenon sunlight simulator (LSS-55) with a test source meter (Keithley 2450) at a simulated AM 1.5 G (100 mW·cm^{-2}) light intensity. The *J–V* curves were measured from −0.02 V to 0.70 V with a step size of 5 mV and no wait time. The EQE of the devices was measured using a quantum efficiency test system (LST-QE).

Reporting summary

Further information on research design is available in the Nature Portfolio Reporting Summary linked to this article.

Data availability

All data generated or analysed during this study are included in the published article and its Supplementary Information. Additional data are available from the corresponding authors on request. Source data are provided with this paper.

References

1. Jin, X. et al. Controllable solution-phase epitaxial growth of Q1D $Sb_2(S,Se)_3$/CdS heterojunction solar cell with 9.2% efficiency. *Adv. Mater.* **33**, 2104346 (2021).
2. Chen, S. et al. Simultaneous band alignment modulation and carrier dynamics optimization enable the highest efficiency in Cd-free Sb_2Se_3 solar cells. *Adv. Funct. Mater.* **34**, 2403934 (2024).
3. Zhou, Y. et al. Thin-film Sb_2Se_3 photovoltaics with oriented one-dimensional ribbons and benign grain boundaries. *Nat. Photonics* **9**, 409–415 (2015).
4. Wang, L. et al. Stable 6%-efficient Sb_2Se_3 solar cells with a ZnO buffer layer. *Nat. Energy* **2**, 17046 (2017).
5. Dong, J. et al. Carrier management through electrode and electron-selective layer engineering for 10.70% efficiency antimony selenosulfide solar cells. *Nat. Energy* **10**, 857–868 (2025).
6. Chen, J. et al. Se-elemental concentration gradient regulation for efficient $Sb_2(S,Se)_3$ solar cells with high open-circuit voltages. *Angew. Chem. Int. Ed.* **63**, e202409609 (2024).
7. Tang, R. et al. Heterojunction annealing enabling record open-circuit voltage in antimony triselenide solar cells. *Adv. Mater.* **34**, 2109078 (2022).
8. Liu, C. et al. Heterojunction lithiation engineering and diffusion-induced defect passivation for highly efficient $Sb_2(S,Se)_3$ solar cells. *Energy Environ. Sci.* **17**, 8402–8412 (2024).
9. Li, J. et al. Hydrazine hydrate-induced surface modification of CdS electron transport layer enables 10.30%-efficient $Sb_2(S,Se)_3$ planar solar cells. *Adv. Sci.* **9**, 2202356 (2022).
10. Liu, A. et al. KCl treatment of CdS electron-transporting layer for improved performance of $Sb_2(S,Se)_3$ solar cells. *ACS Appl. Mater. Inter.* **15**, 48147–48153 (2023).
11. Gu, Y. et al. Solvent annealing enabling reconstruction of cadmium sulfide film for improved heterojunction quality and photovoltaic performance of antimony selenosulfide solar cells. *Adv. Funct. Mater.* **34**, 2311577 (2024).
12. Xue, D.-J. et al. Regulating strain in perovskite thin films through charge-transport layers. *Nat. Commun.* **11**, 1514 (2020).
13. Zhong, S. et al. Mitigating plasmonic absorption losses at rear electrodes in high-efficiency silicon solar cells using dopant-free contact stacks. *Adv. Funct. Mater.* **30**, 1907840 (2020).
14. Yang, X. et al. High-performance TiO_2-based electron-selective contacts for crystalline silicon solar cells. *Adv. Mater.* **28**, 5891–5897 (2016).
15. Xing, C. et al. Electron-selective strontium oxide contact for crystalline silicon solar cells with high fill factor. *Sol. RRL* **7**, 2201100 (2023).
16. Wang, F. et al. Interface dipole-induced field-effect passivation for achieving 21.7% efficiency and stable perovskite solar cells. *Adv. Funct. Mater.* **31**, 2008052 (2021).
17. Yang, Y. et al. Inverted perovskite solar cells with over 2000 h operational stability at 85 °C using fixed charge passivation. *Nat. Energy* **9**, 37–46 (2024).
18. Zhang, D. et al. Mitigated front contact energy barrier for efficient and stable perovskite solar cells. *Energy Environ. Sci.* **17**, 3848–3854 (2024).
19. Wan, Y. et al. Tantalum oxide electron-selective heterocontacts for silicon photovoltaics and photoelectrochemical water reduction. *ACS Energy Lett.* **3**, 125–131 (2018).
20. Deo, M. et al. Tantalum oxide as an efficient alternative electron transporting layer for perovskite solar cells. *Nanomaterials* **12**, 780 (2022).
21. Huang, W.-C. et al. Boosting kesterite solar cell performance with tantalum oxide passivation layer and in situ formed point contacts. *Sol. RRL* **8**, 2301039 (2024).
22. Sahoo, K. K., Pradhan, D., Ghosh, S. P., Gartia, A. & Kar, J. P. Modulation of electrical properties of sputtered Ta_2O_5 films by variation of RF power and substrate temperature. *Phys. Scr.* **99**, 025934 (2024).
23. Li, K. et al. Molecular beam epitaxy deposition of in situ O-doped CdS films for highly efficient $Sb_2(S,Se)_3$ solar cells. *Adv. Funct. Mater.* **33**, 2304141 (2023).
24. Che, B. et al. Post-deposition treatment of Sb_2Se_3 enables defect passivation and increased carrier transport dimension for efficient solar cell application. *Angew. Chem. Int. Ed.* **64**, e202425639 (2025).
25. Dai, G. et al. Selenium-rich $Sb_2(S,Se)_3$ thin films deposited via sequential chemical bath deposition for high-efficiency solar cells. *Adv. Funct. Mater.* **35**, 2415215 (2025).
26. Noh, Y. S. et al. Characteristics of MIS capacitors using Ta_2O_5 films deposited on ZnO/p-Si. *Microelectron. Eng.* **66**, 637–642 (2003).
27. Novkovski, N. & Atanassova, E. Charge trapping during constant current stress in Hf-doped Ta_2O_5 films sputtered on nitrided Si. *Thin Solid Films* **519**, 2262–2267 (2011).
28. Cunha, J. M. V. et al. Perovskite metal–oxide–semiconductor structures for interface characterization. *Adv. Mater. Interfaces* **8**, 2101004 (2021).
29. Chen, C. et al. 6.5% Certified efficiency Sb_2Se_3 solar cells using PbS colloidal quantum dot film as hole-transporting layer. *ACS Energy Lett.* **2**, 2125–2132 (2017).
30. Wang, X., Tang, R., Wu, C., Zhu, C. & Chen, T. Development of antimony sulfide–selenide $Sb_2(S,Se)_3$-based solar cells. *J. Energy Chem.* **27**, 713–721 (2018).
31. Tang, R. et al. Hydrothermal deposition of antimony selenosulfide thin films enables solar cells with 10% efficiency. *Nat. Energy* **5**, 587–595 (2020).
32. Shen, G. et al. Strong chelating additive and modified electron transport layer for 8.26%-efficient Sb_2S_3 solar cells. *Adv. Energy Mater.* **15**, 2406051 (2025).
33. Liu, G. et al. Multidentate chelation heals structural imperfections for minimized recombination loss in lead-free perovskite solar cells. *Angew. Chem. Int. Ed.* **61**, e202209464 (2022).
34. Chen, P. et al. Buried interface engineering-assisted defects control and crystallization manipulation enable stable perovskite solar cells with efficiency exceeding 25%. *Adv. Funct. Mater.* **34**, 2409497 (2024).

35. Wu, T. et al. Heat treatment in an oxygen-rich environment to suppress deep-level traps in Cu_2ZnSnS_4 solar cell with 11.51% certified efficiency. *Nat. Energy* **10**, 630–640 (2025).
36. Liu, X. et al. Enhanced Sb_2Se_3 solar cell performance through theory-guided defect control. *Prog. Photovolt.* **25**, 861–870 (2017).
37. Zhao, Y. et al. Energy band alignment and defect synergistic regulation enable air-solution-processed kesterite solar cells with the lowest V_{OC} deficit. *Adv. Mater.* **37**, 2409327 (2025).
38. Liang, X. et al. Reduction of bulk and interface defects via photo-annealing treatment for high-efficiency antimony selenide solar cells. *Energy Environ. Sci.* **17**, 9499–9508 (2024).
39. Wen, X. et al. Vapor transport deposition of antimony selenide thin film solar cells with 7.6% efficiency. *Nat. Commun.* **9**, 2179 (2018).
40. Lazanas, A. C. & Prodromidis, M. I. Electrochemical impedance spectroscopy-a tutorial. *ACS Meas. Sci. Au* **3**, 162–193 (2023).
41. Chen, J., Seo, J.-Y. & Park, N.-G. Simultaneous improvement of photovoltaic performance and stability by in situ formation of 2D perovskite at $(FAPbI_3)_{0.88}(CsPbBr_3)_{0.12}$/CuSCN interface. *Adv. Energy Mater.* **8**, 1702714 (2018).
42. Abbas, M. et al. Highest solar-to-hydrogen conversion efficiency in Cu_2ZnSnS_4 photocathodes and its direct unbiased solar seawater splitting. *Nano Micro Lett.* **17**, 257 (2025).
43. Chen, J., Zhao, X., Kim, S.-G. & Park, N.-G. Multifunctional chemical linker imidazoleacetic acid hydrochloride for 21% efficient and stable planar perovskite solar cells. *Adv. Mater.* **31**, 1902902 (2019).
44. Chen, S. et al. A Cd-free electron transport layer simultaneously enhances charge carrier separation and transfer in Sb_2Se_3 photocathodes for efficient solar hydrogen production. *Adv. Funct. Mater.* **35**, 2420912 (2025).
45. Shi, X. et al. Nanorod-textured $Sb_2(S,Se)_3$ bilayer with enhanced light harvesting and accelerated charge extraction for high-efficiency $Sb_2(S,Se)_3$ solar cells. *Chem. Eng. J.* **437**, 135341 (2022).
46. Li, Z. et al. 9.2%-efficient core-shell structured antimony selenide nanorod array solar cells. *Nat. Commun.* **10**, 125 (2019).
47. Zhang, Y. et al. Selenium-graded $Sb_2(S_{1-x}Sex)_3$ for a planar heterojunction solar cell delivering a certified power conversion efficiency of 5.71%. *Sol. RRL* **1**, 1700017 (2017).
48. Wang, W. et al. Over 6% certified $Sb_2(S,Se)_3$ solar cells fabricated via in situ hydrothermal growth and postselenization. *Adv. Electron. Mater.* **5**, 1800683 (2019).
49. Chen, S. et al. A codoping strategy for efficient planar heterojunction Sb_2S_3 solar cells. *Adv. Energy Mater.* **12**, 2202897 (2022).

Acknowledgements

This work is financially supported by the National Natural Science Foundation of China (52402104, C.L.), the Natural Science Foundation of Guangxi Province (2024GXNSFBA010280, C.L.), the National Key R&D Program of China (grant no. 2024YFB4205104, Y.M.) and the Guangxi Science and Technology Major Project (AA23073018, B.Z.).

Author contributions

A.G. and C.L. conceived the study and designed the experiments. A.G., J.Y., S.Y., and R.Y. fabricated the devices. B.L., Y.W., and K.S. were responsible for device performance and film morphology characterization. Q.X. carried out TA measurements. A.G., Z.L., and J.W. characterized and analyzed the various photoelectric properties. A.G. and C.L. co-wrote the paper. B.Z. and Y.M. revised the manuscript.

Competing interests

The authors declare no competing interests.

Additional information

Supplementary information The online version contains supplementary material available at https://doi.org/10.1038/s41467-025-67334-y.

Correspondence and requests for materials should be addressed to Cong Liu, Jing Wang, Bingsuo Zou or Yaohua Mai.

Peer review information *Nature Communications* thanks Peng Wang, Yi Zhang, and the other anonymous reviewer(s) for their contribution to the peer review of this work. A peer review file is available.